

# Synchrotron-based X-ray Fluorescence Ghost Imaging

MATHIEU MANNI<sup>1,2</sup>, ADI BEN-YEHUDA<sup>2</sup>, YISHAY KLEIN<sup>2</sup>, BRATISLAV LUKIC<sup>1</sup>, ANDREW KINGSTON<sup>3</sup>, ALEXANDER RACK<sup>1</sup>, SHARON SHWARTZ<sup>2,\*</sup>, AND NICOLA VIGANÒ<sup>1,4,\*\*</sup>

<sup>1</sup>ESRF — The European Synchrotron, Grenoble, 38043, France

<sup>2</sup>Physics Department and Institute of Nanotechnology and Advanced Materials, Bar Ilan University, Ramat Gan, 52900, Israel

<sup>3</sup>Department of Materials Physics, Research School of Physics, The Australian National University, Canberra, ACT 2601, Australia

<sup>4</sup>IRIG-MEM, CEA, Université Grenoble Alpes, Grenoble, 38000, France

\* Co-corresponding author: sharon.shwartz@biu.ac.il

\*\* Co-corresponding author: nicola.vigano@cea.fr

Compiled June 29, 2023

**X-ray Fluorescence Ghost Imaging (XRF-GI) was recently demonstrated for x-ray lab sources. It has the potential to reduce acquisition time and deposited dose by choosing their trade-off with spatial resolution, while alleviating the focusing constraints of the probing beam. Here, we demonstrate the realization of synchrotron-based XRF-GI: We present both an adapted experimental setup and its corresponding required computational technique to process the data. This not only extends the above mentioned advantages to synchrotron XRF imaging, it also presents new possibilities for developing strategies to improve precision in nano-scale imaging measurements.** © 2023 Optica Publishing Group

<http://dx.doi.org/10.1364/ao.XX.XXXXXX>

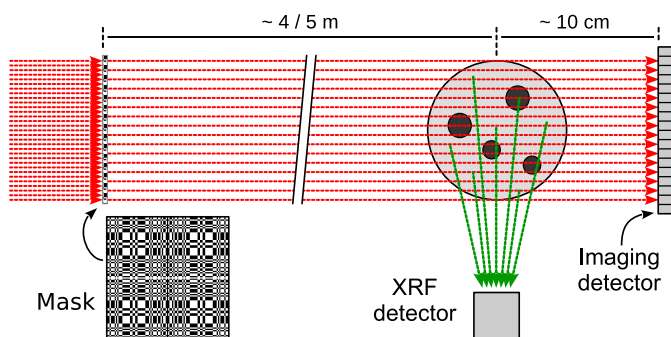
## A. Introduction

X-ray fluorescence (XRF) is used in a wide variety of experimental techniques, including two-dimensional and three-dimensional chemical mapping spanning a large range of scales. It is used for sample characterization in a multitude of application areas, including material science [1], chemistry [2], and cultural heritage [3]. The chemical sensitivity of XRF is achieved through the excitation of core electrons: When the excited atoms return to lower excitation states, they emit secondary photons with characteristic energies, that uniquely depend on the atomic number. Energy-resolving detectors (routinely used in x-ray measurements), can discriminate these photons with sufficient energy resolution, to identify the element from which it originated. XRF imaging is usually achieved by scanning the samples with a focused beam (pencil beam), and by collecting the emitted XRF signal (spectrum) with single-pixel energy-resolving detectors. The collected XRF spectra are then processed, to fit the measured local chemical composition [4].

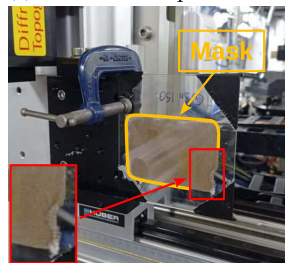
Pencil beam acquisitions require raster-scanning (sequentially) of all the points in the field of view (FoV). Each exposure has an associated XRF spectrum, which corresponds to a single-pixel in the resulting spectral image. In contrast, classical Ghost

Imaging (GI) acquisitions illuminate the entire FoV with different structured beams at each exposure. For x-rays, these structured beams are usually obtained by inserting non-configurable transversely-displaced structuring masks in the beam, to encode the spatial information in the acquired GI signals. For XRF-GI, the XRF detector records the spectrum associated with each illumination pattern. The XRF energy emission lines corresponding to different chemical elements are computationally reconstructed into spatially resolved maps, using the mask shapes and advanced computational imaging algorithms [5]. Synchrotron radiation, compared to x-ray tube based sources, is characterized by higher photon flux and (on long beamlines) spatial coherence. This enables reaching x-ray beam waists of tens of *nm* [6], which enable the study of micro- and nano-structured samples with unrivaled resolutions and speeds, compared to laboratory sources. On the other hand, it also delivers a high radiation dose rate per unit-surface per unit-time, which can cause serious localized damage and deformation in sensitive samples. Heat can also contribute to positional drifts and uncertainties, potentially leading to image degradation. By spreading the beam flux over the entire FoV (as opposed to just the focal spot in pencil beam), XRF-GI could potentially help mitigate dose effects in a more efficient manner (e.g. easier cooling), and reduce the localized radiation-induced damage. Thus, despite having first developed XRF-GI on laboratory equipment, the transposition to synchrotron beamlines is highly desirable.

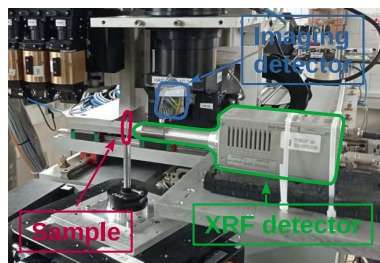
X-ray GI image reconstructions require the masks and the incident beam (intensity and shape) to be known. If the beam intensity is not constant, its changes are especially detrimental when they are higher than the intensity variation introduced by the masks. In that case, they can be tracked with a beam monitor. The masks can be known with one of the following approaches: Measuring the masks in advance (Computational GI); splitting the structured beam with a beam-splitter positioned after the masks, and measuring the beam that does not impinge on the sample (Classical GI) [7–9], or simply by knowing the mask design from fabrication. Here, we demonstrate a synchrotron-based XRF-GI implementation that does not require knowing or measuring the masks in advance, to split the structured beam (Fig. 1a), nor using a beam monitor to track possible incident



(a) Schematic setup



(b) Mask



(c) Sample &amp; detectors

**Fig. 1.** (a) Schematic synchrotron XRF-GI setup; (b) CuSn mask, whose corner is shown in the inset on the bottom left; and, (c) sample, imaging detector with Si attenuation wafers, and XRF detector.

beam intensity variations.

## B. Experimental setup

The proposed setup is presented in Fig. 1. A large structuring mask is positioned on a translation stage in the x-ray beam upstream of the sample. At each GI realization, the synchrotron x-ray beam only illuminates a portion of the mask, producing the corresponding illuminating beam shape. Different beam shapes are obtained by translating the mask transversely with respect to the incoming beam. A 2D imaging detector is positioned downstream of the sample, and an XRF single-pixel detector is positioned next to the sample, perpendicular to the incoming beam direction.

We have demonstrated the proposed setup on the ID19 beamline of the ESRF — The European Synchrotron, using a  $1 \times 2 \text{ mm}^2$  incident beam size. The imaging detector was a so-called Hasselblad system, with two identical lenses (100 mm focal length) in tandem configuration (giving  $\sim \times 1$  magnification), with a  $500 \mu\text{m}$  LuAG:Ce scintillator and a “pco.edge 5.5” camera. It was positioned  $\sim 10 \text{ cm}$  downstream of the sample, with an effective pixel size of  $6 \mu\text{m}$ . A large CuSn mask was positioned  $\sim 4 - 5 \text{ m}$  upstream of the sample. The incoming beam energy was  $\sim 26 \text{ keV}$ , given by the beamline’s single-harmonic undulator (type: u13). The XRF detector was a “Vortex 90EX” single-pixel detector, controlled by a “FalconX” module. The sample is composed of two Cu flattened wires and one Fe  $50 \mu\text{m}$  thick wire, stored in a capillary. The capillary is mostly made of plastic, with heavier trace elements.

## C. Acquisition procedure

In [5], the imaging and XRF detectors acquired their respective signals separately. In fact, the sample needed to be removed from the FoV to acquire the beam structures. Thus, the same scan was performed two times, one with the sample in the FoV, using the XRF detector, and one without the sample in the

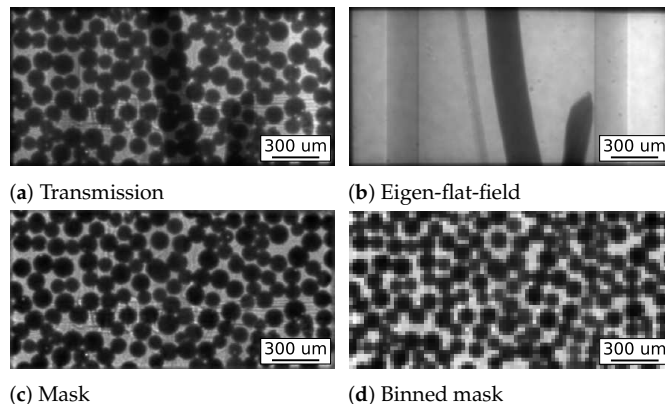


**Fig. 2.** (a) Transmission image of the sample with the masks; (b) eigen-flat-field computed from the stack of transmission images; (c) the extracted mask from transmission; and, (d) its  $4 \times 4$  binned version. The intensity gradient in (a) and (b) is due to the fact that the sample was not correctly positioned in the center of the beam. This effect is correctly taken into account by the eigen-flat-field subtraction when retrieving (c).

FoV, using the imaging detector. This exposed one of the two measurements to positioning and flux estimation errors with respect to the other. In this new implementation, the two detectors simultaneously acquire their respective signals (for the same time duration). In other words, each XRF signal is concurrently acquired with its corresponding beam structure, in the same flux and positioning conditions, and the imaging detector records the transmitted signal through both sample and mask for each GI realization. We then separate the beam structure from the sample shape computationally, during the data processing. Both implementations require measuring the intensity distribution of the impinging beam on the masks. This is done either at the beginning or the end of the scan.

The required exposure times of the high-resolution imaging and XRF detectors are usually different: The imaging detector is exposed to the direct (intense) beam, and therefore saturates well before the required SNR is met for the XRF signal. We circumvent this by acquiring many shorter acquisitions (e.g. exposures of  $0.1 \text{ s}$  each) for each same mask position, and accumulating them. Here, we translated the large mask both vertically and horizontally, acquiring 16 and 56 positions respectively. This amounts to 896 total GI realizations. We exposed 32 times for each GI realization for  $0.1 \text{ s}$ , amounting to  $3.2 \text{ s}$  of cumulative realization exposure time.

## D. Data processing

GI is a computational imaging technique, and it requires several computational steps to recover real-space images. Our implementation requires an additional step to decouple the structure of the incoming beam from the sample transmission, and to retrieve the normalization coefficients for the incoming beam intensity variations. In this section, we describe the additional step, which is unique to our proposed setup. The full GI data processing pipeline is described in Sec. E of the supplemental material.

If we assume that the sample transmission does not change throughout the GI acquisition, it is possible to decouple the sample transmission from the beam structure through principal component analysis (PCA). Let us represent the sample transmission with the vector  $\underline{f}$  (which also includes the spatial beam intensity profile), the beam structures for each GI realization

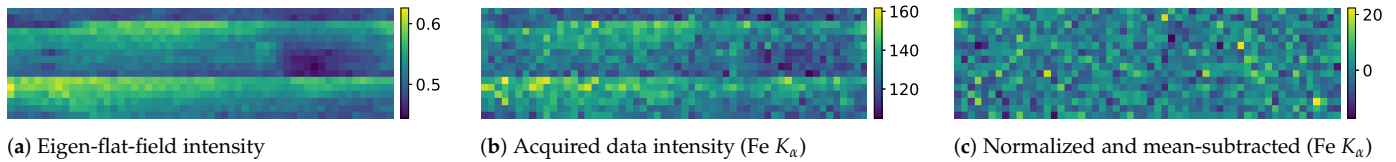


**Fig. 3.** (a) Integrated intensities of the eigen-flat-fields; (b) acquired intensities of the GI realizations for the Fe  $K_\alpha$  line; and, (c) normalized and mean-subtracted intensities for the Fe  $K_\alpha$  line.

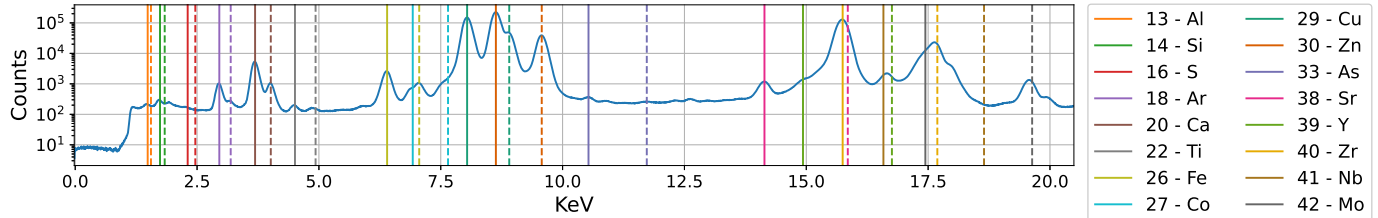


**Fig. 4.** XRF spectrum of the studied sample. Solid and dashed lines indicate  $K_\alpha$  and  $K_\beta$  emission lines, respectively.

as the set of vectors  $M = \{\underline{m}_j\}$ , where  $j \in [1, K]$  is the index of each GI realization and  $K$  is the total number of realizations, and the beam intensity for each realization with the set of coefficients  $C = \{c_j\}$ . For each realization, the transmission of the sample plus the structured beam is  $\underline{t}_j = c_j \underline{f} \otimes \underline{m}_j$ , where  $\otimes$  is the element-wise vector product (defined in the supplementary material). The average of all transmission images is  $\frac{1}{K} \sum_j^K \{c_j \underline{f} \otimes \underline{m}_j\} = \underline{f} \otimes \frac{1}{K} \sum_i^K c_i \underline{m}_i$ . The masks in the set  $M$  are supposed to be uncorrelated with each other, and  $\underline{f}$  is the only component present in each transmission image  $\underline{t}_j$ . Thus, it is the dominant component in the PCA of the matrix  $T = [\underline{t}_1, \underline{t}_2, \dots, \underline{t}_K]$ . If we split the highest PCA component from the others, and reconstruct these two sets separately, we will obtain  $c_j \underline{f}$  (called eigen-flat-field) from the former set, and  $\underline{m}_j$  from the latter set, for each GI realization  $j$ .

We show an example of transmission  $\underline{t}$  in Fig. 2a, the corresponding eigen-flat-field in Fig. 2b and beam structure in Fig. 2c. The intensity fluctuations  $c_j$  are computed by integrating each eigen-flat-field  $c_j \underline{f}$ , where  $\sum_i f_i$  with  $i \in [1, N]$  is the sum of all the pixels  $i$  in the image  $\underline{f}$ , and resulting in a constant multiplicative factor. The integrated intensities in Fig. 3a are in good agreement with the low-frequency trend of the corresponding Fe  $K_\alpha$  values in Fig. 3b. We normalize the values in Fig. 3b by the computed intensities in Fig. 3a, subtract the mean, and obtain the corrected GI realization intensities in Fig. 3c.

The GI reconstruction pixel size is determined through the auto-correlation (AC) function of the structured beams [10]. Supposing that the mask is not periodic and sampled over non-overlapping regions, the resulting structured beams are not correlated with each other. Thus, it is enough to compute the AC of each structured beam with itself. The selected GI reconstruction pixel size is the lowest half-width half-maximum (HWHM) of all the AC curves. More details can be found in the supplemental material. In the presented experiment, we found a minimum HWHM equal to 4 imaging detector pixels: Given its pixel size of  $6 \mu\text{m}$ , it is equivalent to a  $24 \mu\text{m}$  GI pixel size. Therefore, we binned the mask images  $4 \times 4$ , as shown in Fig. 2d.

The GI reconstruction is performed with the Primal-Dual Hybrid Gradient (PDHG) algorithm, and using the  $l_1$ -norm minimization of the isotropic Total Variation (TV) of the image [11]. The weight of the TV term is selected through cross-validation [12]. The data processing code can be found at [13].

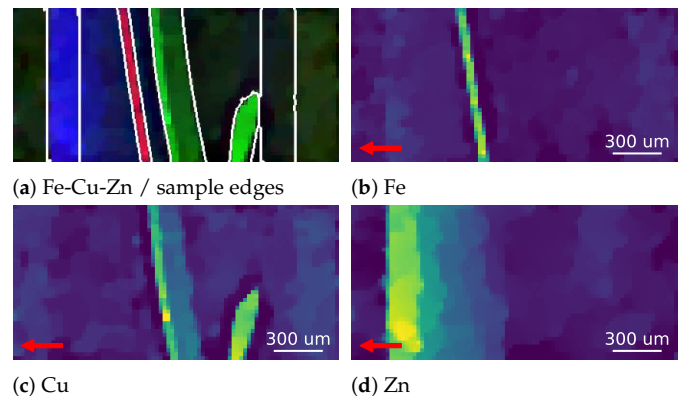


**Fig. 5.** (a) Composite image of Fe, Cu, Zn (Red, Green, and Blue respectively), and super-imposed edges of the transmission image in Fig. 2b; and the elemental reconstructions of: (b) Fe; (c) Cu; and, (d) Zn. The images are affected by self-attenuation of the XRF photons. The XRF detector position is indicated with a red arrow.

## E. Results

The XRF spectrum of the analyzed sample is shown in Fig. 4. The Fe and Cu peaks from the wires are clearly visible. The C  $K_\alpha$  line of the plastic capillary is below the detection limit of the XRF detector, but lines of other elements can be seen, e.g. Zn. In Fig. 5, we find the GI reconstructions of the Fe, Cu, and Zn XRF signals in the FoV (Fig. 5b, Fig. 5c, and Fig. 5d respectively). In Fig. 5a, we present a color-coded composite image of the Fe, Cu, and Zn XRF signals (Red, Green, and Blue respectively), with super-imposed edges from Fig. 2b. This figure shows that the elemental images are in good agreement with the corresponding expected objects in the transmission image: The spatial distribution of the elements is correctly recovered (aside from artifacts). The two main types of artifacts are: (a) trace signals from other channels; and (b) self-attenuation. Point (a) means that the signal for one XRF line can have long tails in its energy dispersion function, and its signal can be mistakenly associated with other XRF lines. As a result, reconstructions show faint features from other elements. For instance, the Fe reconstruction (Fig. 5b) shows traces of the capillary on the left-most part of the FoV. Point (b) means that the sample attenuates some of the XRF photons that it emits. As a result, regions of the

sample further away from the detector have a much lower signal than regions of the sample closer to the XRF detector. This effect is clearly visible in both the Cu and Zn reconstructions (Fig. 5c, and Fig. 5d). More specifically, the biggest Cu wire is reconstructed with a higher signal on its left side, and only the leftmost part of the capillary is reconstructed. The XRF detector is in fact positioned on the left side of the images, as seen by the transmission detector (indicated with a red arrow in Figs. 5b to 5d). This type of artifact is common to all XRF methods.

The reconstructed images are approximately  $1 \times 2 \text{ mm}^2$  in size, which corresponds to  $42 \times 87$  pixels (for  $24 \mu\text{m}$  pixel size). The acquisition consisted of  $16 \times 56$  GI realizations, which represent  $\sim 24.52\%$  of the reconstructed pixels.

## F. Impact & Outlook

The proposed implementation is robust against mask positioning errors or drifts, because the structure of the beam is acquired in line with the sample (without beam splitting), and simultaneously with the XRF signal. This also implies a simplified setup, with fewer sources of noise or misalignment, compared to beam-splitter-based setups. Optionally, the masks can be mapped beforehand with a higher spatial resolution or longer exposure. The inline images obtained during the XRF-GI acquisition can then be used to register the high-quality masks with the XRF-GI data. Compared to XRF pencil beam scanning, this XRF-GI implementation is also robust with respect to image distortions arising from drifts during a single image. The deriving improved stability and precision could have its biggest impact at the nano-scale, where tracking drifts and positioning errors is of vital importance to reduce image distortions.

The lab-based XRF-GI demonstrated in [5] assumes a constant flux from the x-ray source (or the flux to be directly measurable upstream to the sample), and the positions of the masks to not undergo drifts during the measurement of the XRF signal. These are valid assumptions for lab x-ray sources coupled with detectors with pixel sizes in the order of the tens of  $\mu\text{m}$ . X-ray tubes (used in laboratory x-ray setups) are characterized by rather stable emission fluxes over time, while synchrotron sources exhibit beam intensity decay. Even in top-up mode, it is possible to observe up to 10% flux variations. Beam monitors are usually placed upstream of the focusing optics and/or masks. The masks create unknown and variable attenuation between the diode and the sample, which renders calibration of the XRF signal difficult or impossible. Moreover, on synchrotron beamlines, cameras with sub- $\mu\text{m}$  or few  $\mu\text{m}$  pixel sizes are routinely used. Thus, with slight instability of the beam direction (e.g. drifts of reflecting x-ray optics visible due to the long lever arm at a beamline) and sample drifts, misalignment artefacts are more likely to manifest. The implementation presented here directly addresses these limitations, and renders XRF-GI applicable on synchrotron beamlines.

Enabling synchrotron-based XRF-GI has a direct impact on every technique that leverages the XRF signal. As an example, XAS (x-ray absorption spectroscopy) can use XRF as a high-quality proxy for the absorption signal. With XRF-GI, it becomes possible to obtain spatial information from XAS measurements, without the need to radically change a beamline layout with respect to beam shaping and sample positioning. More precisely, our XRF-GI implementation only requires minor changes to pre-existing setups: Adding a two-dimensional detector downstream of the sample, and a translation stage for scanning the masks. Importantly, the translation of the masks does not require high precision or reproducibility. A pencil

beam setup would instead require introducing slits and focusing optics in the beam, while ensuring mechanical precision much finer than the beam size. Thus, XRF-GI will open new possibilities in existing beamlines and techniques, that were not originally designed to provide spatial XRF information. Moreover, this technique could also be used with laboratory sources, to extend [5].

XRF-GI can also be used in conjunction with XRF pencil beam scanning. GI could deliver a preliminary low-resolution map of the sample, with much fewer exposures than the number of pixels, by using compressive sensing (CS) [12]. Pencil beam scanning would then be used to obtain high resolution and high signal-to-noise ratio acquisitions of selected regions of interest. The resulting acquisition times and deposited dose would be lower than the full high-resolution pencil beam scan.

While the presented technique is a simple and robust way to perform XRF-GI on a synchrotron beamline, it could be further improved. In particular, it requires to have enough photons in every pixel of the transmitted images: Both the object and the mask need to be transparent enough to provide enough signal on the imaging detector. This limitation on the sample can be relaxed, by scanning the mask beforehand. In fact, even in the case where some regions of the sample were to fully attenuate the transmitted beam, the transmission of one region of the mask in each GI realization would be enough to retrieve the correct position of the mask for the reconstruction. This would also relax the dependency on the eigen-flat-field determination step.

**Funding.** PAZY Foundation; Australian Research Council (Discovery project, DP210101312).

**Acknowledgments.** AK acknowledges support from the Australian Research Council through funding of the Discovery Project DP210101312. This research was supported by the Pazy Foundation. NV acknowledges fruitful discussion and feedback from K. Joost Batenburg and Daniele Pelliccia.

**Disclosures.** The authors declare no conflicts of interest.

**Data availability.** Data underlying the results are available at [14].

**Supplemental document.** See Supplement 1 for supporting content.

## REFERENCES

1. A. Chirilă, S. Buecheler, F. Pianezzi, P. Bloesch, C. Gretener, A. R. Uhl, C. Fella, L. Kranz, J. Perrenoud, S. Seyrling, R. Verma, S. Nishiwaki, Y. E. Romanyuk, G. Bilger, and A. N. Tiwari, *Nat. Mater.* **10**, 857 (2011).
2. J. Lim, Y. Li, D. H. Alsem, H. So, S. C. Lee, P. Bai, D. A. Cogswell, X. Liu, N. Jin, Y.-s. Yu, N. J. Salmon, D. A. Shapiro, M. Z. Bazant, T. Tylliszczak, and W. C. Chueh, *Science* **353**, 566 (2016).
3. R. Ploeger and A. Shugar, *Science* **354**, 826 (2016).
4. V. Solé, E. Papillon, M. Cotte, P. Walter, and J. Susini, *Spectrochimica Acta Part B: At. Spectrosc.* **62**, 63 (2007).
5. Y. Klein, O. Sefi, H. Schwartz, and S. Shwartz, *Optica* **9**, 63 (2022).
6. J. Cesar da Silva, A. Pacureanu, Y. Yang, S. Bohic, C. Morawe, R. Barrett, and P. Cloetens, *Optica* **4**, 492 (2017).
7. R. S. Bennink, S. J. Bentley, and R. W. Boyd, *Phys. Rev. Lett.* **89**, 113601 (2002).
8. D. Pelliccia, A. Rack, M. Scheel, V. Cantelli, and D. M. Paganin, *Phys. Rev. Lett.* **117**, 113902 (2016).
9. A. Gatti, E. Brambilla, M. Bache, and L. A. Lugiato, *Phys. Rev. Lett.* **93**, 093602 (2004).
10. A. M. Kingston, G. R. Myers, D. Pelliccia, F. Salvemini, J. J. Bevil, U. Garbe, and D. M. Paganin, *Phys. Rev. A* **101**, 053844 (2020).

11. E. Y. Sidky, J. H. Jørgensen, and X. Pan, *Phys. Med. Biol.* **57**, 3065 (2012).
12. T. J. Lane and D. Ratner, *Opt. Express* **28**, 5898 (2020).
13. <https://github.com/cicwi/PyCorrectedEmissionCT>.
14. <https://doi.org/10.5281/zenodo.7828494>.

## FULL REFERENCES

1. A. Chirilă, S. Buecheler, F. Pianezzi, P. Bloesch, C. Gretener, A. R. Uhl, C. Fella, L. Kranz, J. Perrenoud, S. Seyrling, R. Verma, S. Nishiwaki, Y. E. Romanyuk, G. Bilger, and A. N. Tiwari, "Highly efficient Cu(In,Ga)Se<sub>2</sub> solar cells grown on flexible polymer films," *Nat. Mater.* **10**, 857–861 (2011).
2. J. Lim, Y. Li, D. H. Alsem, H. So, S. C. Lee, P. Bai, D. A. Cogswell, X. Liu, N. Jin, Y.-s. Yu, N. J. Salmon, D. A. Shapiro, M. Z. Bazant, T. Tyliczszak, and W. C. Chueh, "Origin and hysteresis of lithium compositional spatiodynamics within battery primary particles," *Science* **353**, 566–571 (2016).
3. R. Ploeger and A. Shugar, "Where science meets art," *Science* **354**, 826–828 (2016).
4. V. Solé, E. Papillon, M. Cotte, P. Walter, and J. Susini, "A multiplatform code for the analysis of energy-dispersive X-ray fluorescence spectra," *Spectrochimica Acta Part B: At. Spectrosc.* **62**, 63–68 (2007).
5. Y. Klein, O. Sefi, H. Schwartz, and S. Shwartz, "Chemical element mapping by x-ray computational ghost fluorescence," *Optica* **9**, 63 (2022).
6. J. Cesar da Silva, A. Pacureanu, Y. Yang, S. Bohic, C. Morawe, R. Barrett, and P. Cloetens, "Efficient concentration of high-energy x-rays for diffraction-limited imaging resolution," *Optica* **4**, 492 (2017).
7. R. S. Bennink, S. J. Bentley, and R. W. Boyd, "'two-photon' coincidence imaging with a classical source," *Phys. Rev. Lett.* **89**, 113601 (2002).
8. D. Pelliccia, A. Rack, M. Scheel, V. Cantelli, and D. M. Paganin, "Experimental X-Ray Ghost Imaging," *Phys. Rev. Lett.* **117**, 113902 (2016).
9. A. Gatti, E. Brambilla, M. Bache, and L. A. Lugiato, "Ghost imaging with thermal light: Comparing entanglement and classical correlation," *Phys. Rev. Lett.* **93**, 093602 (2004).
10. A. M. Kingston, G. R. Myers, D. Pelliccia, F. Salvemini, J. J. Bevitt, U. Garbe, and D. M. Paganin, "Neutron ghost imaging," *Phys. Rev. A* **101**, 053844 (2020).
11. E. Y. Sidky, J. H. Jørgensen, and X. Pan, "Convex optimization problem prototyping for image reconstruction in computed tomography with the Chambolle-Pock algorithm," *Phys. Med. Biol.* **57**, 3065–3091 (2012).
12. T. J. Lane and D. Ratner, "What are the advantages of ghost imaging? Multiplexing for x-ray and electron imaging," *Opt. Express* **28**, 5898 (2020).
13. <https://github.com/cicwi/PyCorrectedEmissionCT>.
14. <https://doi.org/10.5281/zenodo.7828494>.